
A Three-Dimensional Velocity of an Erupting Prominence Prior to a Coronal Mass Ejection

Maria V. GUTIERREZ^{1,2*}, **Kenichi OTSUJI^{3,4}**, **Ayumi ASAI⁴**, **Raul TERRAZAS⁵**,
Mutsumi ISHITSUKA², **Jose ISHITSUKA^{2†,6}**, **Naoki NAKAMURA⁴**, **Yusuke**
YOSHINAGA⁷, **Satoshi MORITA⁸**, **Takako T. ISHII⁴**, **Satoru UENO⁴**, **Reizaburo**
KITAI^{9,10,4} **and Kazunari SHIBATA^{4,10}**

¹Institute for Research in Astronomy and Astrophysics (IAFE CONICET-UBA), Buenos Aires, Argentina

²Geophysical Institute of Peru, Lima, Peru

³National Institute of Information and Communications Technology (NICT), Koganei, Tokyo, 184-8795, Japan

⁴Astronomical Observatory, Kyoto University, Sakyo, Kyoto, 606-8502, Japan

⁵Ica Solar Station, Department of Physics, San Luis Gonzaga National University of Ica, Ica, Peru

⁶National University of the Center of Peru, Huancayo, Peru

⁷Department of Astronomy, Kyoto University, Sakyo, Kyoto, 606-8502, Japan

⁸National Astronomical Observatory of Japan, Osawa, Mitaka, Tokyo, 181-8588, Japan

⁹Bukkyo University, Kita, Kyoto, 603-8301, Japan

¹⁰Ritsumeikan University, Kita, Kyoto, 603-8577, Japan

¹¹Doshisha University, Kyotanabe, Kyoto, 610-0394, Japan

*E-mail: mvgutierrez@iafe.uba.ar

Received ; Accepted 2021 January 8

Abstract

We present a detailed three-dimensional (3D) view of a prominence eruption, coronal loop expansion, and coronal mass ejections (CMEs) associated with an M4.4 flare that occurred on 2011 March 8 in the active region NOAA 11165. Full-disk $H\alpha$ images of the flare and filament ejection were successfully obtained by the Flare Monitoring Telescope (FMT) following its re-

location to Ica University, Peru. Multiwavelength observation around the $H\alpha$ line enabled us to derive the 3D velocity field of the $H\alpha$ prominence eruption. Features in extreme ultraviolet were also obtained by the Atmospheric Imager Assembly onboard the *Solar Dynamic Observatory* and the Extreme Ultraviolet Imager on board the *Solar Terrestrial Relations Observatory - Ahead* satellite. We found that, following collision of the erupted filament with the coronal magnetic field, some coronal loops began to expand, leading to the growth of a clear CME. We also discuss the succeeding activities of CME driven by multiple interactions between the expanding loops and the surrounding coronal magnetic field.

Key words: Sun: chromosphere — Sun: flares — Sun: filaments, prominences — Sun: coronal mass ejections (CMEs)

1 Introduction

Solar flares are explosive events occurring in the solar corona that release extremely large quantities (10^{28} – 10^{32} erg) in radiative, kinetic, thermal and non-thermal form. They are considered to be one of the most attractive scientific objects in solar physics, with emissions across the electromagnetic spectrum originating from atmospheric layers extending from the chromosphere, in extreme cases the photosphere, to the outer regions of the solar corona. Solar flares can also produce high-speed coronal mass ejections (CMEs) that travel through interplanetary space with occasional serious impacts on the solar-terrestrial environment.

A filament, relatively cool, dens plasma supported by magnetic field and floated in the corona, sometimes erupts and cause or be part of a CME. Therefore, the relations among filament eruptions, flares and CMEs have been earnestly studied (e.g., Schmieder et al. 2013; Schmieder et al. 2015; Schmieder et al. 2020). Munro et al. (1979) reported that more than 70 % of CMEs are associated with eruptive prominences of filament disappearance, both with and without large soft X-ray (SXR) enhancement, that are accordingly recognized as flares. Gopalswamy et al. (2003) also reported that 72 % of prominence eruptions observed in microwaves are associated with CMEs. Filaments eruptions are thought to be caused by loss of equilibrium and/or magnetohydrodynamic instability (Démoulin and Aulanier 2010; Kliem and Török 2006; Mackay et al. 2010).

Finding the origin of a CME in the solar lower atmosphere and following its evolution to be a CME are, however, sometimes difficult owing to a gap between the coronagraphic observational

[†] This is the former affiliation.

field-of-view of the CME and that for flares and filament eruptions on the solar surface. The flare-CME connection is a controversial topic and of great interest to the scientific community, which has not yet found an established relationship between these phenomena. Some flares, referred to as confined flares, are not eruptive and not associated with CMEs (Moore et al. 2001; Mackay et al. 2010). Some CMEs are not related with flares, which are defined as strong X-ray emission, but related with eruption of quiet region filaments and/or giant arcade formation seen in X-rays (McAllister et al. 1996). Therefore, the connection between a CME and the related phenomena on the solar surface should be cleared more by focusing on the temporal evolution of the flare and its relation to the CME. Accordingly, in this study we investigate the initial phases of CME-related filament eruptions by using $H\alpha$ data with the goal of detecting signatures preceding the launch of CMEs. Recently, a three-dimensional (3D) prominence reconstruction was done by using IRIS data (Schmieder et al. 2017). The authors succeeded to demonstrate that an helical structure of the prominence seen in the IRIS images consists in fact of horizontal field lines parallel to the solar surface. Spectroscopic observations of eruptive filaments have become more important to reveal the relation between CMEs and filament eruptions.

To this end, we examined a set of solar phenomena that occurred on 2011 March 8, in Active Region (AR) NOAA 11165. We examined the erupted prominence in detail and followed its 3D temporal evolution and relation to the overlying coronal magnetic field. The remainder of this paper is organized as follows. We describe the observations in Section 2 and present analysis and results on the prominence eruption and coronal loops prior to the appearance of the CMEs in Sections 3 and 4, respectively. Finally, a summary and discussion are given in Section 5.

2 Observations

On 2011 March 8, an M4.4 solar flare with a soft X-ray (SXR) classification was recorded at AR NOAA 11165, which is located near the southwest solar limb ($S17^\circ$, $W88^\circ$), by the *Geostationary Operational Environmental Satellite (GOES)*. Figure 1 shows the SXR light curves taken by *GOES*. The flare began at 18:08 UT and peaked at 18:28 UT (shown in the figure with arrow 2), with light curves featuring several small humps and subpeaks. This flare was followed by another gradual M1.5 flare that began and peaked at 19:35 and 20:16 UT (arrow 3), respectively.

A filament/prominence eruption associated with the flare can be seen in $H\alpha$ images obtained by the Flare Monitoring Telescope (FMT; Kurokawa et al. 1995), which was originally installed at Hida Observatory, Kyoto University, Japan, and relocated to Ica University, Peru in 2010 under the international collaboration of the Continuous H-Alpha Imaging Network (CHAIN) Project (UeNo et

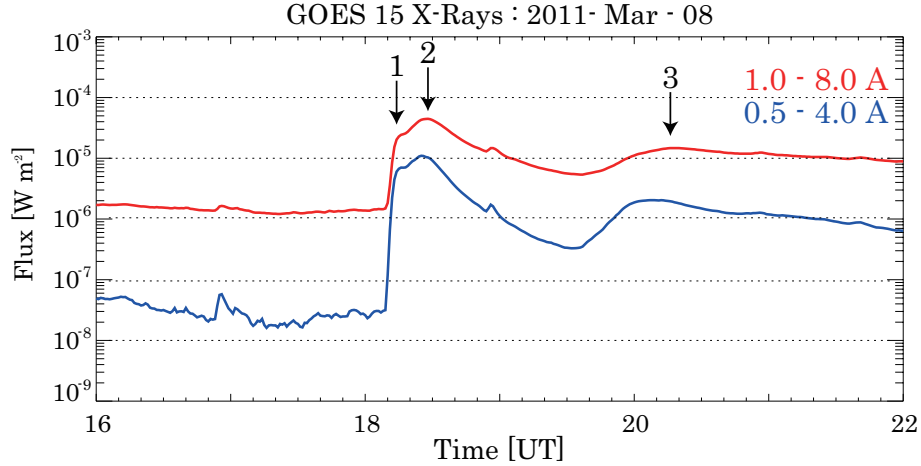


Fig. 1. *GOES* X-ray emission at 1.0 – 8.0 Å (red) and 0.5 – 4.0 Å (blue) channels of the 2011 March 8 flare. Arrow 2 indicates the peak of the M4.4 flare at 18:28 UT. The peak at 20:16 UT corresponds to an M1.5 flare that occurred in the same AR NOAA 11165 (shown with arrow 3).

al. 2007). FMT provides full-disk images in five wavelengths: $H\alpha$ line center (6562.8 Å); wings at $+0.8$ Å and -0.8 Å; continuum (6100 Å) images; and another $H\alpha$ line center image to detect limb prominences. The spatial and temporal samplings of FMT are about $2''.0$, and 20 s, respectively. In this paper, we will use the term ‘FMT-Peru’ to clarify that the data we used in this study were obtained following the relocation.

The telescope is capable of measuring the 3D velocity fields of active filaments/prominences (Morimoto & Kurokawa 2003a; Morimoto & Kurokawa 2003b; Cabezas et al. 2017), and Moreton waves (Eto et al. 2002; Narukage et al. 2002; Narukage et al. 2008; Asai et al. 2012; Cabezas et al. 2019). Figure 2 shows a full-disk $H\alpha$ center image of the flare taken by FMT-Peru, with the erupting feature visible in the region marked with the white box on the southwest limb.

To view the spatial distribution of prominence gases irrespective to line-of-sight motion, we created ‘combined’ images of three wavelengths (center and ± 0.8 Å). Prominences/filaments moving rapidly in the line-of-sight direction are often invisible with images of only one wavelength due to the Doppler shift of the $H\alpha$ line. The images of three wavelengths were, therefore, combined into time series to enable tracking of the evolution of overall prominence gas. At each wavelength, a specific intensity level³ was set and the brighter regions above that level were extracted to reveal the prominences involved in the selected region. Finally, we superimposed the images extracted at the three wavelengths at each time step to produce a time sequence of combined $H\alpha$ images, as shown in the leftmost column of Figure 3. See also the supplementary movie 1 for the temporal evolution of the $H\alpha$ images. It shows images at $H\alpha -0.8$ Å (top left), center (top right), $+0.8$ Å (bottom left), respectively. The bottom right panel is the combined images.

Flare and eruption features were also captured in extreme ultraviolet (EUV) images taken

FMT H α center 6562.8Å 2011-Mar-08 18:14:00 UT

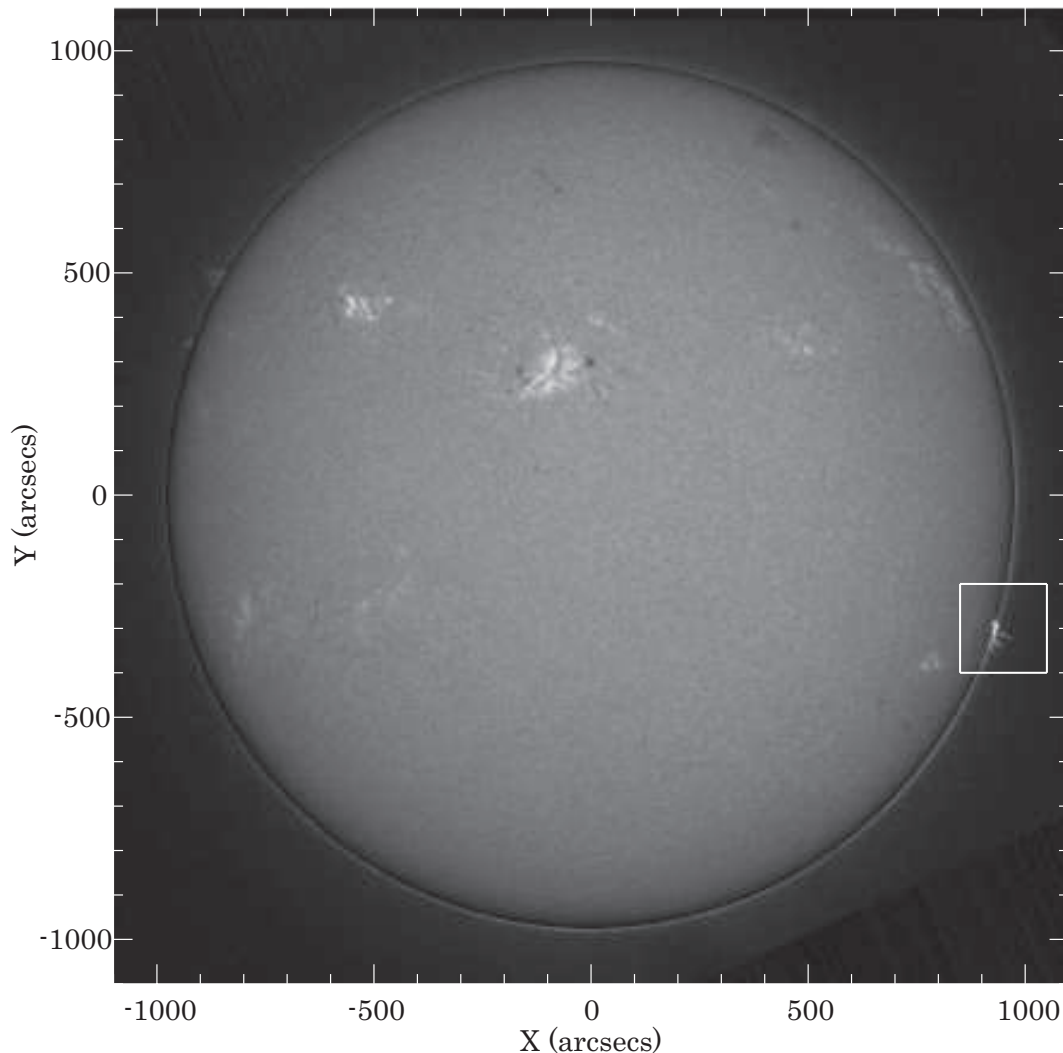


Fig. 2. Full-disk solar image (solar north is up and west is to the right) of the flare in H α center taken at 18:14 UT by FMT-Peru. The white box shows the flaring region of AR NOAA 11165.

by the Atmospheric Imaging Assembly (AIA; Lemen et al. 2012) onboard the *Solar Dynamics Observatory* (SDO; Pesnell et al. 2012). AIA takes full-disk solar images with a temporal resolution of 12 s, while the images of filters 1600 and 1700 Å are taken every 24 s. The pixel size of the images is 0".6. In this study, we used images taken with 304, 171, 193, and 94 Å filter, which are mainly attributable to the He II (80,000K), Fe IX (0.6MK), Fe XII (1.2MK), and Fe XVIII lines (6.3MK), respectively. The second to fifth columns from the left in Figure 3 show the temporal evolution of the flare and the prominence eruption at 304, 171, 193, and 94 Å, respectively.

The prominence eruption associated with the flare is seen as a bright feature in the H α images that moves to the southwest from the flare site. It is also seen as bright features (moving blobs) in the

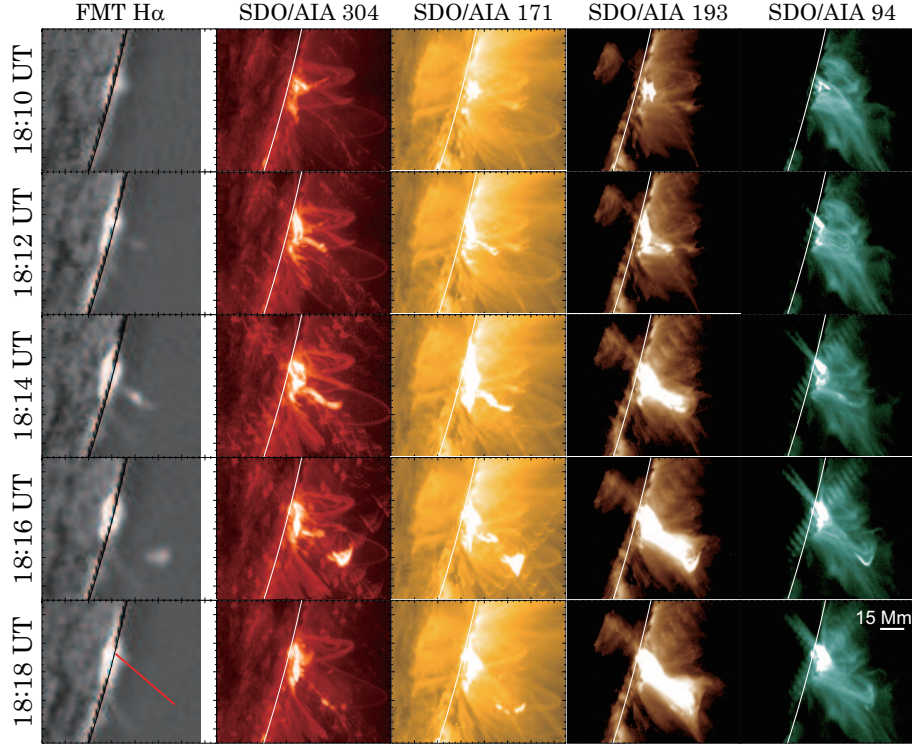


Fig. 3. Multiwavelength time sequences of the 2011 March 8 flare. Columns from left to right are FMT-Peru $H\alpha$ combined, and *SDO/AIA* at 304, 171, 193, and 94 Å images, respectively. The red solid line in the bottom left panel indicates the slit position used in Figure 7.

AIA 304 and 171 Å images. In particular, common features are seen on the erupting blobs in the $H\alpha$, EUV 304 and 171 Å images. By contrast, in the AIA 193 and 94 Å images outer coronal loops with higher temperature are predominant. As is often observed (Chifor et al. 2006), the erupting filament suffers heating at the outer edge and is therefore visible even in EUV bands such as 171 and 193 Å, which are sensitive to higher temperatures. Here, we have to note that the AIA channels have broad temperature response. It is often difficult to know whether a structure is really hot or cool. After 18:16 UT, the prominence becomes unclear in both $H\alpha$ and 304 Å, while the coronal loops visible in 193 and 94 Å are still evolving and brightening.

The Extreme-Ultraviolet Imager (EUVI; Wuelser et al. 2004), part of the Sun-Earth Connection Corona and Heliospheric Investigation (SECCHI; Howard et al. 2008) onboard the *Solar Terrestrial Relations Observatory - Ahead (STEREO-A)* (Kaiser et al. 2008), also observed the flare and prominence eruption (filament eruption in the view of *STEREO-A*) in the EUV bands. At the time of observation, *STEREO-A* was located $87.^\circ 6$ ahead of the Earth on a heliocentric elliptical orbit in the ecliptic plane and, therefore, was able to capture a top view of the flaring region (NOAA 11165). We used 171 Å EUVI images in which the emission line of Fe IX (0.6MK) was dominant to compare the temporal evolution of the erupting blobs.

The flare and prominence eruption were followed by a CME, which was first seen at 19:00 UT in the field of view of coronagraph C2 on the Large Angle and Spectrometric COronagraph (LASCO; Brueckner et al. 1995) onboard *SOHO*. We will discuss this CME further in Section 4.

To examine the temporal evolution and dynamics of the flare and prominence eruption, we used hard X-ray (HXR) data obtained by the *Reuven Ramaty High Energy Solar Spectroscopic Imager* (*RHESSI*; Lin & Rhesi Team 2002) and microwave data taken at the Sagamore Hill Solar Observatory under the Radio Solar Telescope Network (RSTN; Guidice & Eadon 1981). We focused in particular on 25 – 50 and 50 – 100 keV HXR emissions measured by *RHESSI* and microwave emissions at the 4.99, 8.8, and 15.4 GHz channels measured by RSTN. At these wavelengths (in this case given, respectively, as energy bands and frequencies) it is possible to observe nonthermal Bremsstrahlung and gyrosynchrotron emissions associated with accelerated electrons, allowing for the examination of the energetic features of accelerated electrons in the flare.

3 3D Velocity Field of the Prominence Eruption

There have been some reports on the derivation of the Doppler (line-of-sight) velocities of $H\alpha$ disk filaments observed using FMT (Morimoto & Kurokawa 2003a; Morimoto & Kurokawa 2003b; Cabezas et al. 2017). The methods used in these studies are based on the ‘cloud model’, which was originally suggested by Beckers (1964) and Mein & Mein (1988) and modified for FMT data. By contrast, in this study we observed an off-limb bright prominence with a dark background, which meant that we could not use the cloud-model-based methods.

Instead, to derive Doppler velocities we assumed that the observed profiles were emitted from a slab with a uniform and constant source function. Based on the three wavelength data points ($H\alpha$ center and $\pm 0.8 \text{ \AA}$) and an additional assumption that the $H\alpha$ intensities at the $\pm 4.0 \text{ \AA}$ wings are equal to zero, profile fitting produced four unknown parameters (i.e., the source function, optical depth, Doppler velocity, and Doppler width) with an error of about $\pm 10 \text{ km s}^{-1}$. Owing to misalignment of the wavelengths of Peru-FMT filters from their nominal values, the actual error in determined Doppler velocity was potentially worse at roughly $\pm 15 \text{ km s}^{-1}$. Furthermore, FMT-Peru cannot detect blobs with velocities greater than 50 km s^{-1} . We, in this paper, fitted the erupting filament only with images of the $H\alpha$ center and the wings with the band position of $\pm 0.8 \text{ \AA}$ and with the passband width of about 0.5 \AA . Profiles of prominences observed with spectrographs often show a narrow $H\alpha$ line with a maximum FWHM between 0.6 and 0.8 \AA (Ruan et al. 2018). In our case the wide bandpass of the filters around 0.5 \AA allows us to integrate the prominence emission from the inflexion point of the line profile (0.45 \AA) to the far wing. Therefore, the prominences are visible in our three filters, while

there is a large uncertainty in the Doppler shift values.

The left panels of Figure 4 show temporal evolution maps of Doppler velocity with blue and red colors indicating blue- and red-shifted Doppler velocities, respectively. The erupting blob initially has a red-shift with a velocity of about 25 km s^{-1} that changes at around 18:14 UT to a blue-shift with a velocity of about 30 km s^{-1} . This timing (18:14 UT) corresponds to arrow 1 in Figure 1.

By assuming that the observed $H\alpha$ prominence is optically thin, it is possible to combine the optical thickness and the source function into one unknown parameter – the emissivity – and reduce the number of unknown physical parameters to three. We derived the Doppler velocities by fitting the data under this assumption and then confirmed that the resulting velocities were consistent with those derived with the former method. The Doppler velocities in the remainder of the study were therefore derive using the former method.

We derived the tangential velocity of the ejected filament (i.e., the velocity of the filament in the plane of the sky) by applying the local correlation tracking (LCT) method to the $H\alpha$ combined image sequence. The right panels of Figure 4 show the temporal evolution maps of the tangential velocity, with the green arrows showing the direction and amplitude of the tangential velocity. The tangential velocity of the erupting filament is roughly 80 km s^{-1} and rapidly decelerating. The direction of the tangential velocity changes from southwest to slightly northwest at around 18:14 UT, corresponding temporally to the sudden direction change of the Doppler velocity.

Because the flare site was nearly on the solar limb ($W88^\circ$), *STEREO-A*, which was located $87.^\circ6$ ahead of the Earth at the time of observation, was able to capture a top view of the flare and the filament eruption. As discussed above, the erupting $H\alpha$ prominence was co-spatial with a bright blob seen in the AIA 171 \AA images (see Figure 3), and therefore we investigated the temporal evolution of the filament eruption in the *STEREO-A/SECCHI/EUVI* 171 \AA images. Figure 5 shows the temporal evolution of the erupting filament in the EUVI 171 \AA images. The contours outline a bright feature (bright blob) associated with the erupting filament, with different colors indicating different times. It is seen that the filament predominantly moves southward, with a slight westward motion before 18:14 UT, followed by eastward motion afterwards. These motions correspond to motion away from and toward the Earth, respectively. The centroid of the contoured region moves at roughly 40 km s^{-1} between 18:12:15 UT (red) and 18:13:30 UT (yellow) and at 40 km s^{-1} between 18:14:45 UT (green) and 18:16:00 UT (blue).

Analysis of the blob dynamics in the prominence eruption reveal an interesting behavior in which the blobs are deflected at specific heights within the corona, indicating an interaction between the blobs and the coronal environment. In the next section, we examine the reactions consequential to this interaction.

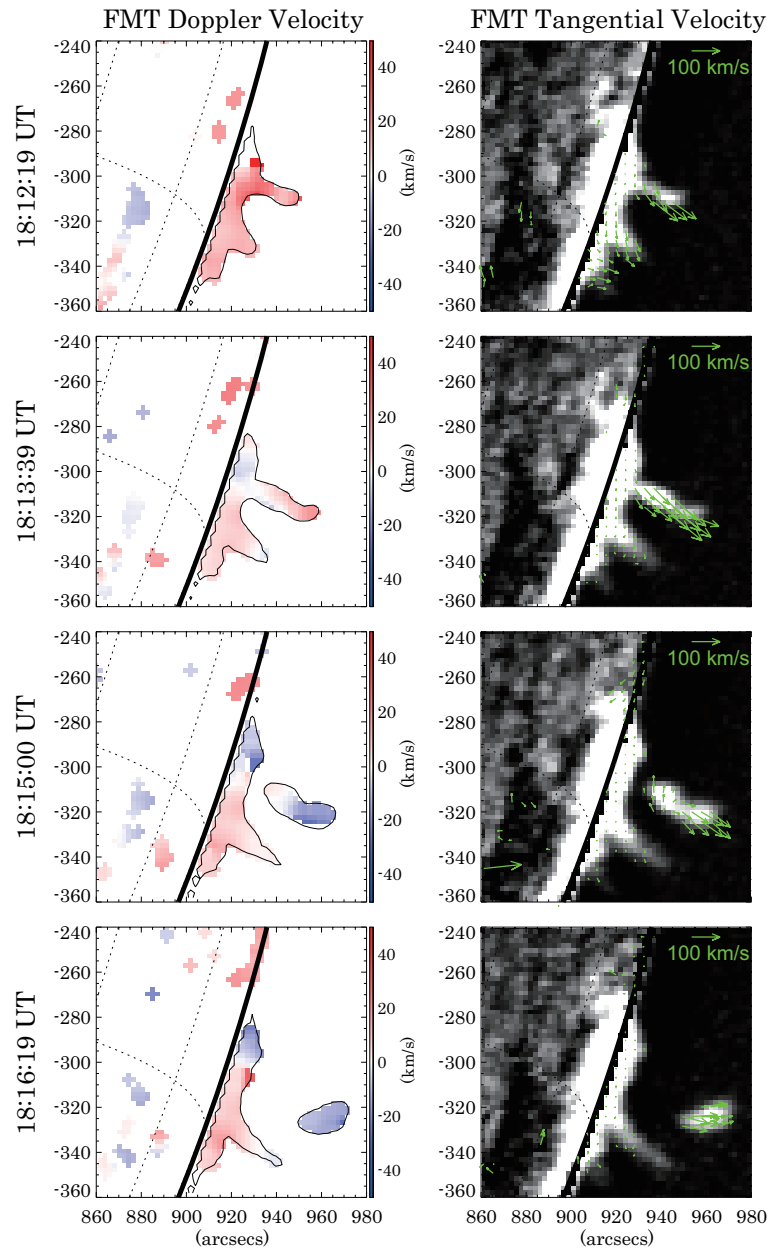


Fig. 4. Temporal evolution of 3D velocity of erupting prominence. *Left:* Doppler velocity shown with blue- and red-shifted features colored blue and red, respectively. *Right:* Tangential velocity with direction and magnitude indicated with green arrows. The background images are FMT-Peru H α combined images. The sign of the Doppler shift changes from red to blue at around 18:14 UT; at the same time, the direction of the tangential velocity changes from southwest to slightly northwest.

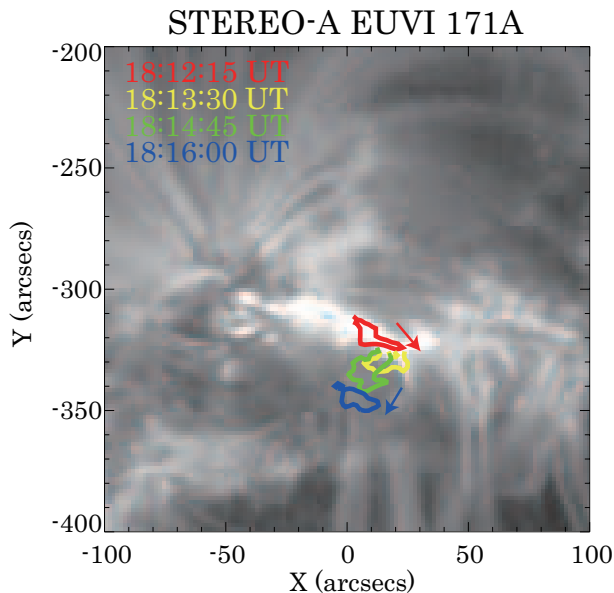


Fig. 5. Temporal evolution of filament eruption seen in the *STEREO-A*/SECCHI/EUVI 171 Å images. The contours show the bright feature associated with the erupting filament, with different colors indicating different times. The background is an EUVI 171 Å image taken at 18:11 UT

4 EUV Flux Rope Expansion and CME

Following the disappearance of the cool $H\alpha$ prominence at around 18:18 UT, further activity commences in the higher corona, in the form of expansion of the outer coronal loops seen in the SDO/AIA 94 Å band. This activity appears to lead to a CME. Figure 6 shows the temporal evolution of the expanding loops. From 18:10 UT onward, the expansion of a coronal loop is seen (Loop1). After 18:19 UT, another loop (Loop2) begins to expand from just south of Loop1. Loop1 remains in place or expand very slowly, and disappears at 18:35 UT. On the other hand, Loop2 rapidly expands until it eventually leaves the field of view.

To study the temporal evolution of the vertical motion of these activities in more detail, we constructed the time slice diagrams (time-sequenced images along slit lines) shown in the bottom panels of Figure 7. Panels (c) and (d) show time slice diagrams for the coronal loops of AIA 94 Å (negative images) and the $H\alpha$ prominence, respectively. The zero of the vertical axis on each panel corresponds to the lower edge of the slit line (i.e., the edge closer to the solar limb). The positions of the slits are also shown in Figure 6(i) and in the bottom left panel of Figure 3. As described in Section 3, the $H\alpha$ prominence erupts and decelerates after 18:14 UT prior to fading out at around 18:18 UT. The vertical motion of the EUV 94 Å loop (Loop1) is seen to be associated with the $H\alpha$ prominence eruption. Loop1 also shows rapid acceleration and sudden deceleration corresponding to motions in the $H\alpha$ prominence eruption. The Loop1 and $H\alpha$ prominence ascending velocities of

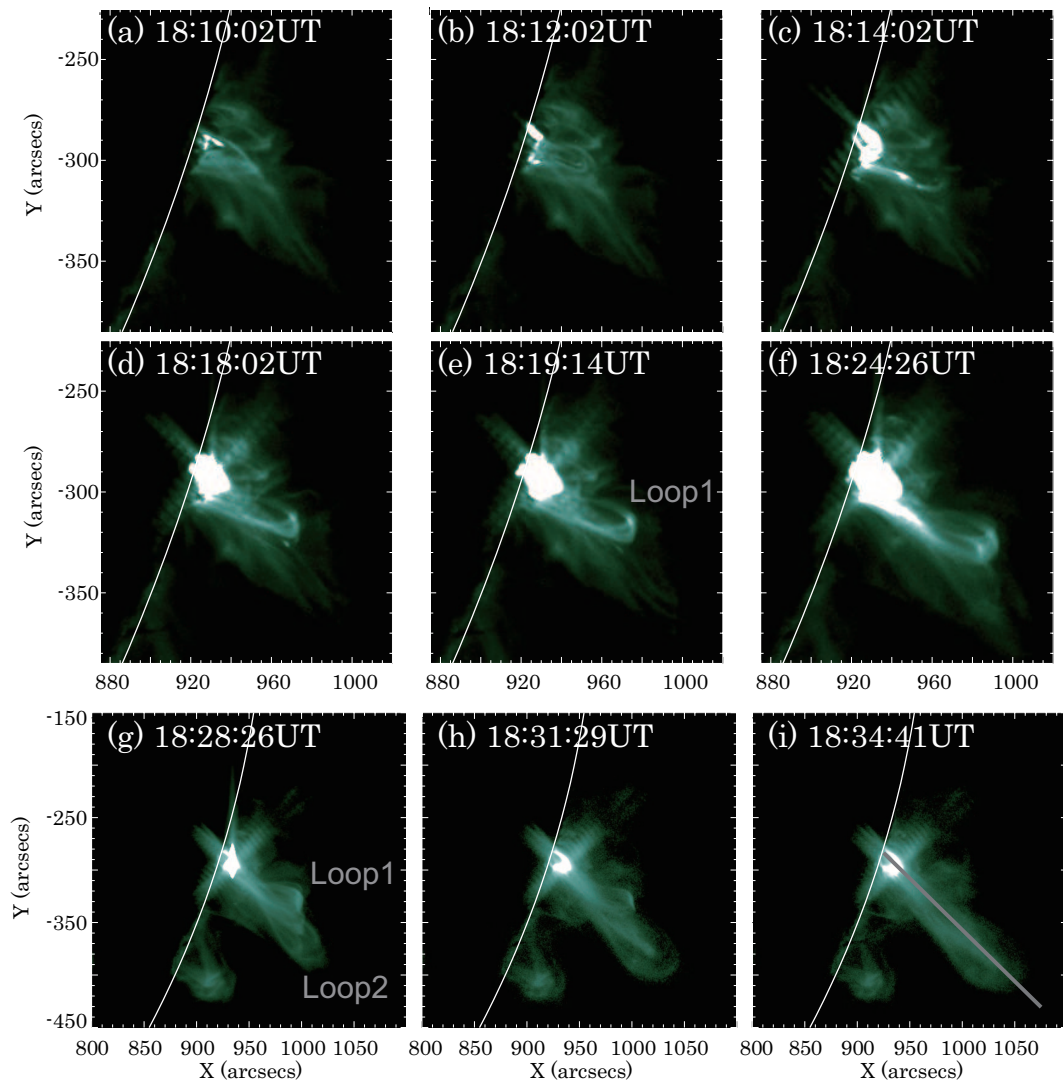


Fig. 6. Temporal evolution of expanding loops seen in the *SDO/AIA* 94 Å images. Note that the field of view of panels (g) to (i) is wider than that from (a) to (f). The gray solid line in panel (i) indicates the slit position used in Figure 7.

about 130 and 100 km s⁻¹, respectively. After 18:19 UT, another vertical motion associated with Loop2 is seen in the time slice diagram of the EUV 94 Å images. The ascending velocity in this case is about 120 km s⁻¹.

Figures 7(a) and (b) show the light curves at SXR (1.0 – 8.0 and 0.5 – 4.0 Å) taken by *GOES*, HXR (25 – 50 and 50 – 100 keV) taken by *RHESSI*, and microwaves (4.99, 8.8, and 15.4 GHz) taken by RSTN. In the HXR and microwave light curves two bursts, with peaks at 18:12 – 18:14 and at 18:19 – 18:20 UT, are seen. The short-lived nature of these features and the simultaneity of the emissions suggest that both the microwave and HXR emissions are of nonthermal origin. The timings of these nonthermal bursts are associated with the rapid eruptions of H α prominence and EUV coronal loops. The temporal association between the vertical motion (i.e., outward rapid acceleration) and the

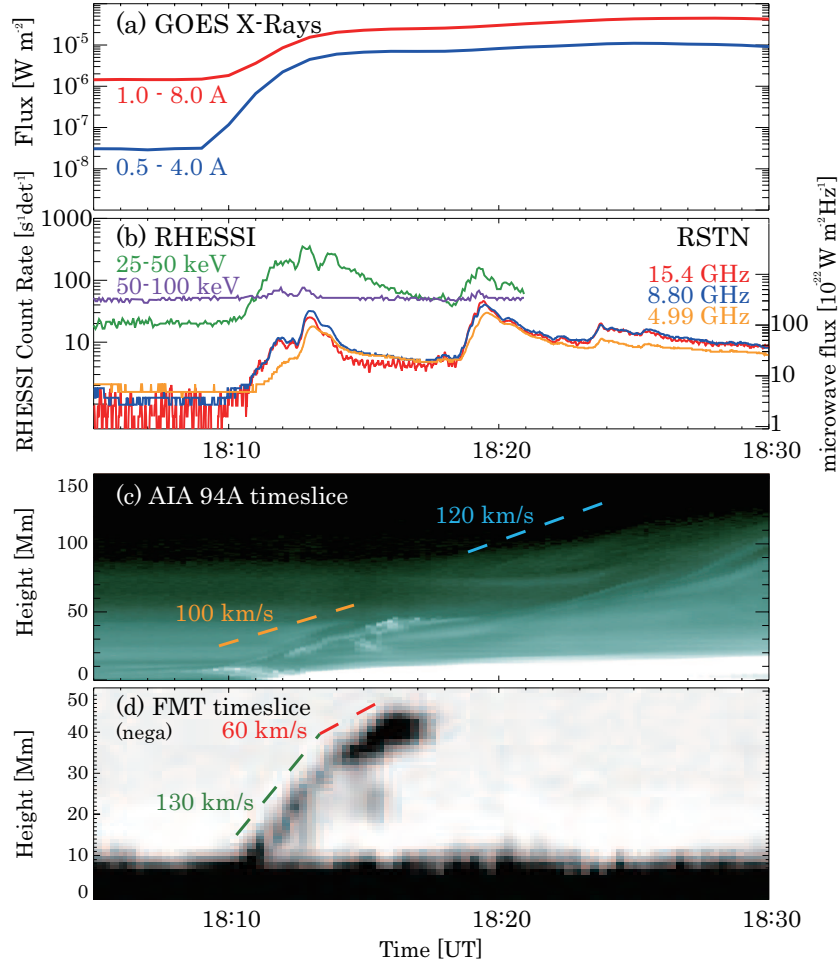


Fig. 7. (a) Soft X-ray light curves in the *GOES* 1.0 – 8.0 (red) and 0.5 – 4.0 Å (blue) channels. (b) Hard X-ray light curves measured with *RHESSI* at 25 – 50 (green) and 50 – 100 keV (purple) and microwave flux taken with *RSTN* in the 4.99 (orange), 8.8 (blue), and 15.4 (red) channels. (c) Time-sequenced EUV (94 Å) image (time slice diagram) obtained with *SDO/AIA* along the slit line shown in Figure 6(i). (d) Time slice diagram of $H\alpha$ combined image obtained with *FMT-Peru* along the slit line shown in the bottom left panel of Figure 3. The zeros of the vertical axis for both time-slice diagrams correspond to the lower edges of the slit lines.

nonthermal emissions indicates that plasmoids are being ejected with the release of high amounts of magnetic energy as has previously been reported (e.g., Kahler et al. 1988; Ohyama & Shibata 1998; Asai et al. 2004; Asai et al. 2006; Nishizuka et al. 2010; Takasao et al. 2016). These results support the so-called ‘plasmoid-induced-reconnection’ model (Shibata 1999; Shibata & Tanuma 2001).

Figure 8 shows spatial distributions of emission sources in HXR for the nonthermal bursts around at 18:13 UR (Fig. 8a) and 18:19 UT (Fig. 8b). The backgrounds are *AIA* 94 Å images are taken at 18:13:02 and 18:19:02 UT, respectively. We overlaid HXR contour images observed with *RHESSI* in 12 – 25 keV (red) and 40 – 80 keV (yellow). The levels of the contours are 40%, 60%, 80%, and 95% of the peak intensity. We synthesized the HXR images by using grids 3 – 8 and integrating over 40 seconds for the first peak and 80 seconds for the second peak. We recognize a

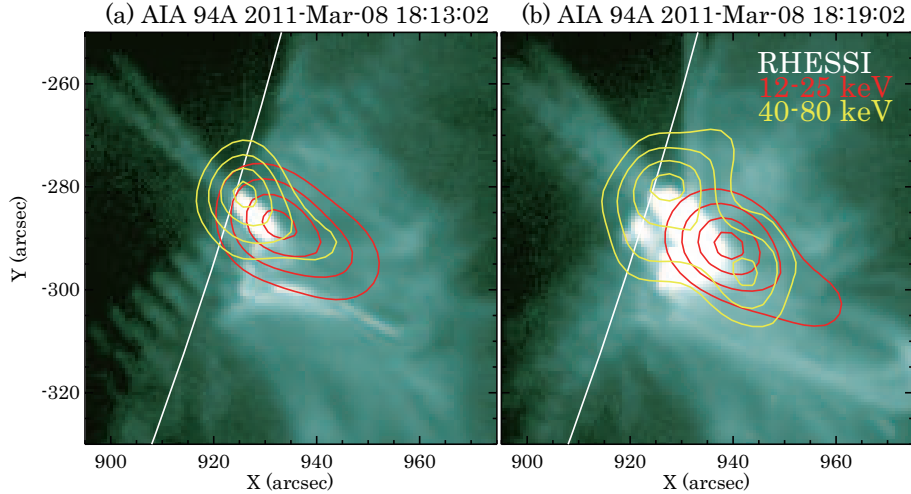


Fig. 8. Spatial distribution of the emission sources. The backgrounds are AIA 94 Å images taken at 18:13:02 (a) and 18:19:02 UT (b). The contours show the *RHESSI* 12 – 25 keV intensity (red), and the 40 – 60 keV intensity (yellow), respectively. The contour levels are 40, 60, 80, and 95% of the peak intensity.

HXR emission source in the low energy band (12 – 25 keV) appear above the flare loops seen in the 94 Å images in the both times. These emission sources extend in the vertical direction, i.e. along the current sheet. The HXR emission in the high energy band (40 – 80 keV), on the other hand, mainly comes from the footpoint of the flare loops. These are consistent with the previous study (Su et al. 2012). We can also see a “loop-top” HXR emission source (Masuda et al. 1994) or an extension of the contour line in the high energy HXR band. These loop-top HXR emission sources are located just above the top of the bright flare loops seen in the 94 Å, and are probably associated with the interaction between the reconnection outflow jet and/or plasmoid ejected from the reconnection region and the flare loops (Takasao et al. 2016).

The *SOHO/LASCO* C2 coronagraph detected the appearance of a faint and slow CME at 19:06 UT with a linear velocity of 280 km s^{-1} (see the *SOHO/LASCO* CME online catalog, http://cdaw.gsfc.nasa.gov/CME_list/) (Yashiro et al. 2004). From the timing and direction of expansion, this CME appears to be associated with the flare occurring at 18:30 UT at AR NOAA 11165. Figures 9(a–f) show *LASCO* C2 running difference images of the evolution of the CME, which is referred to hereafter as CME1. After 20:12 UT, another, faster CME (CME2) with a velocity of 700 km s^{-1} appears and follows nearly the same traveling path as that of CME1. From Figures 9(d–f), which show CME2, it is seen that it catches up to and interacts with CME1 in an act of ‘cannibalism’ (Gopalswamy et al. 2001)). Figure 9(g) shows a time-distance diagram of both CMEs and the EUV coronal loop (Loop2). CME2 appears to be associated with the flare starting at 19:45 UT on the same AR.

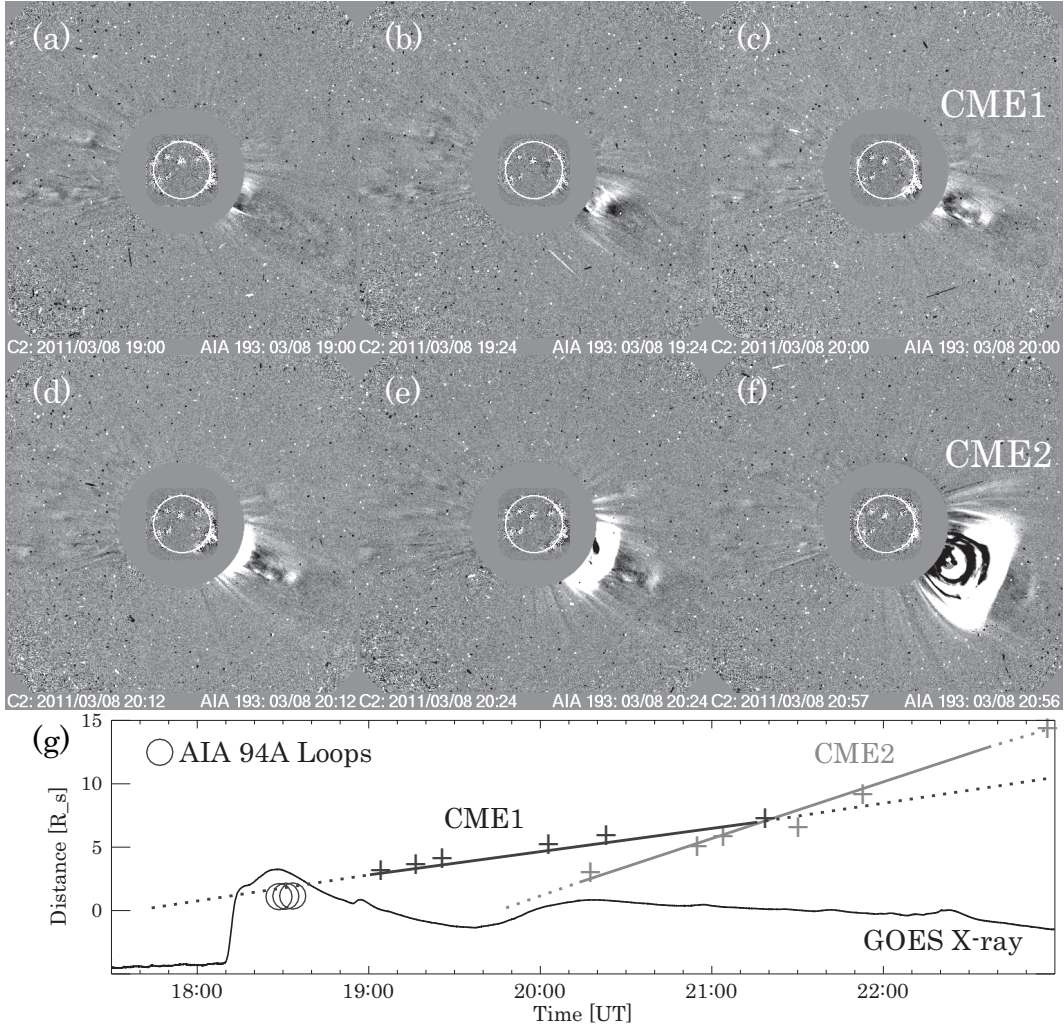


Fig. 9. (a – f) Time sequences of *SOHO*/LASCO C2 running difference images. Each image is overlaid with a corresponding EUV 193 Å running difference image obtained from *SDO*/AIA. (g) Time-distance diagram of CMEs and EUV coronal loops. The distance is measured from the solar limb. The CME front distances for CME1 (CME2) at a given time are represented by black (gray) plus + signs, while the circles ○ mark the position of the EUV coronal loop (Loop2). R_s is the solar radius, ($\approx 695,800$ km. For comparison, we also plot the SXR flux in the *GOES* 1.0 – 8.0 Å channel.

5 Summary and Discussion

In this study, our goal was to investigate the initial phases of CME-related filament eruptions and to detect signatures preceding the launch of a CME. We performed multi-wavelength analyses of the temporal behaviors of the prominence eruption, coronal loop expansion, and CME associated with the M4.4 flare that occurred on 2011 March 8 in AR NOAA 11165. The 3D velocity field of the erupted prominence was derived using the $H\alpha$ data taken by FMT-Peru. The $H\alpha$ prominence accelerated when high amounts of magnetic energy were released, and nonthermal bursts were seen in the microwave (RSTN) and HXR (*RHESSI*) from 18:12 to 18:14 UT, after which the prominence rapidly decelerated in the vertical direction and changed its Doppler velocity direction. Finally, the prominence faded

out. This temporal evolution indicates that the cool material seen in the $H\alpha$ line interacted with the overlying magnetic environment and failed to eject into space. In AIA 304 Å images we can see material falling from there. Therefore, the disappearance of the $H\alpha$ prominence is caused due to decrease of plasma density. The change of direction of the erupted prominence was also captured as a deflection of bright blobs in *STEREO-A/EUVI* 171 Å images, which represents another feature of a confined energy release.

Another energy release associated with the nonthermal emissions occurred just after the confined event (from 18:19 to 18:20 UT). This energy release caused an expansion of coronal loops seen in the *SDO/AIA* 94 Å images (Loop2) and led to a faint CME (CME1). Hours later, another gradual flare and CME (CME2) occurred. Using *SDO/AIA* images, Su et al. (2012) investigated in detail the temporal evolution of the EUV coronal loops associated with the flare in question (i.e., the flare at around 18:10 UT) and the ones associated with another energy release at around 19:45 UT, and interpret the two flares as two stages of a single associated event.

By contrast, we found that the first flare comprised further two-stage energy releases and furthermore, that the initial energy release represented by the $H\alpha$ prominence eruption appears to be confined. Despite this confinement, the energy release triggered another magnetic reconnection followed by the coronal loop expansion and the CME. As Kliem et al. (2020) and Gou et al. (2020) reported, even a confined flare can cause the eruption of an unstable flux rope. In our case, we could not confirm the formation of a flux rope as we were observing a limb flare. Nevertheless, it is possible that dynamic disturbances of the plasmoids and magnetic field triggered further energy release during the course of the event, resulting in multi-stage behavior. On the other hand, as some authors have reported, erupting filaments are often split into sections (Morimoto & Kurokawa 2003b; Tripathi et al. 2006; Guo et al. 2010; Cheng et al. 2018). The blob we observed in $H\alpha$ may be a part of such split filaments and may not be involved at all with the flux rope involved in the CME.

Acknowledgments

The authors acknowledge anonymous referees for their comments and suggestions. The authors are very grateful with all the staff members of the Kwasan and Hida Observatories, Kyoto University of Japan, for all the supports and discussions during the FMT-workshops and working-group meetings conducted in Japan and in Peru. They thank Dr. A. Hillier for his contribution to the FMT-workshops. They also are grateful to *SDO/AIA* and *STEREO/EUVI* teams for providing high quality data used in this study. This work was also supported by the international program “Climate And Weather of the Sun-Earth System - II (CAWSES-II) : Towards Solar Maximum” sponsored by SCOSTEP. This work was also supported by the “UCHUGAKU” project of the Unit of Synergetic Studies for Space, Kyoto University. This work was also supported by JSPS KAKENHI Grant Numbers 25287039, 26400235, 15K17772, and 16H03955. A.A. was supported by a Shiseido Female Researcher Science Grant. The authors would like to thank Enago for the English language review.

References

- Asai, A., Yokoyama, T., Shimojo, M., & Shibata, K. 2004, *ApJL*, 605, L77–L80
- Asai, A., Nakajima, H., Shimojo, M., White S. M., Hudson, H. S., Lin, R. P. 2006, *PASJ*, 58, L1–L5
- Asai, A., Ishii, T. T., Isobe, H., et al.. 2012, *ApJL*, 745, L18
- Beckers, J. M. 1964, PhD Thesis, Univ. Utrecht
- Brueckner, G. E., Howard, R. A., Koomen, M. J., et al. 1995, *Sol. Phys.*, 162, 357
- Cabezas, D. P., Martínez, L. M., Buleje, Y. J., et al. 2017, *ApJ*, 836, id.33
- Cabezas, D. P., Asai, A., Ichimoto, K., et al. 2019, *ApJ*, 883, id.32
- Chen, P. F., & Shibata, K. 2000, *ApJ*, 545, 524
- Cheng, X., Kliem, B., Ding, M. D. 2018, *ApJ*, 856, id.48
- Chifor, C., Mason, H. E., Tripathi, D., et al. 2006, *A&A*, 458, 965–973
- Démoulin, P., and Aulanier, G.. 2010, *ApJ*, 718, 1388–1399
- Eto, S., Isobe, H., Narukage, N., et al. 2002, *PASJ*, 54, 481–491
- Gopalswamy, N., Yashiro, S., Kaiser, M. L., et al. 2001, *ApJL*, 548, L91
- Gopalswamy, N., Shimojo, M., Lu, W., et al. 2003, *ApJ*, 586, 562–578
- Gopalswamy, N., Mikić, Z., Maia, D., et al. 2006, *Space Sci. Rev.*, 123, 303
- Guidice, D. A., & Eadon, E. J. 1981, *BAAS*, 13, 400
- Gou, T., Liu, R., Kliem, B., et al. 2019, *Sci. Adv.*, 5, eaau7004
- Guo, Y., Ding, M. D., Schmieder, B., et al. 2010, *ApJL*, 725, L38–L42
- Howard, R. A., Moses, J. D., Vourlidas, A., et al. 2008, *Space Sci. Rev.*, 136, 67
- Kahler, S. W., Moore, R. L., Kane, S. R., & Zirin, H. 1988, *ApJ*, 328, 824–829
- Kaiser, M. L., Kucera, T. A., Davila, J. M., et al. 2008, *Space Sci. Rev.*, 163, 5
- Kliem, B., and Török, T. 2006, *Phys. Rev. Lett.*, 96, 255002
- Kliem, B., Lee, J., White, S. M., et al. 2020, *ApJ*, submitted
- Kurokawa, H., Kimura, G., Nakai, Y., Kitai, R., Funakoshi, Y., Shinkawa, T. 1995, *J. Geomag. Geoelectr.*, 47, 1043-1052
- Lemen, J. R., Title, A. M., Akin, D. J., et al. 2012, *Sol. Phys.*, 275, 17
- Lin, R. P., & Rhesi Team 2002, *Solar Variability: From Core to Outer Frontiers*, 506, 1035
- Mackay, D. H., Karpen, J. T., Ballester, J. L., et al. 2010 *Space Sci. Rev.*, 151, 333–399
- Masuda, S., Kosugi, T., Hara, H., Tsuneta, S., Ogawara, Y. 1994, *Nature*, 371, 495
- McAllister, A. H., Dryer, M., McIntosh, P., Singer, H., Weiss, L. 1996, *J. Geophys. Res.*, 101, 13497-13516
- Mein, P., & Mein, N. 1988, *A&A*, 203, 162
- Moore, R. L., Sterling, A. C., Hudson, H. S., Lemen, J. R. 2001, *ApJ*, 552, 833-848

Morimoto, T., & Kurokawa, H. 2003a, PASJ, 55, 503-508

Morimoto, T., & Kurokawa, H. 2003b, PASJ, 55, 1141-1151

Munro, R. H., Gosling, J. T., Hildner, E., et al. 1979, Sol. Phys., 61, 201

Narukage, N., Hudson, H. S., Morimoto, T., et al. 2002, ApJL, 572, L109-L112

Narukage, N., Ishii, T. T., Nagata, S., et al. 2008, ApJL, 684, id.L45

Nishizuka, N., Takasaki, H., Asai, A., & Shibata, K. 2010, ApJ, 711, 1062–1072

Ohyama, M., & Shibata, K. 1998, ApJ, 499, 934–944

Pesnell, W. D., Thompson, B. J., & Chamberlin, P. C. 2012, Sol. Phys., 275, 3

Ruan, G., Schmieder, B., Mein, P., et al. 2018, ApJ, 865, id.123

Schmieder, B., Démoulin, P., Aulanier, G. 2013, Adv. Space Res., 51, 1967–1980

Schmieder, B., Aulanier, G., Vršnak, B. 2015, Sol. Phys., 290, 3457–3486

Schmieder, B., Zapiór, M., López Ariste, A., et al. 2017, A&A, 606, id.A30

Schmieder, B., Kim, R.-S., Grison, B. et al. 2020, J. Geophys. Res., 125, A027529

Shibata, K. 1999, Ap&SS, 264, 129

Shibata, K., & Tanuma, S. 2001, Earth Planets Space, 53, 473

Takasao, S., Asai, A., Isobe, H., & Shibata, K. 2016, ApJ, 828, id.103

Tripathi, D., Isobe, H., Mason, H. E. 2006, A&A, 453, 1111–1116

Su, Y., Dennis, B. R., Holman, G. D., et al. 2012, ApJL, 746, L5

UeNo, S., Shibata, K., Kimura, G., et al. 2007, BASI, 35, 697

Wueller, J.-P., Lemen, J. R., Tarbell, T. D., et al. 2004, Proc. SPIE, 5171, 111

Yashiro, S., Gopalswamy, N., Michalek, G., et al. 2004, J. Geophys. Res., 109, A07105